

Banner appropriate to article type will appear here in typeset article

Natural convection in a vertical channel. Part 2. Oblique solutions and global bifurcations in a spanwise-extended domain

Zheng Zheng¹, Laurette S. Tuckerman²† and Tobias M. Schneider¹

¹Emergent Complexity in Physical Systems Laboratory (ECPS), École Polytechnique Fédérale de Lausanne, CH 1015 Lausanne, Switzerland

²Physique et Mécanique des Milieux Hétérogènes (PMMH), CNRS, ESPCI Paris, PSL University, Sorbonne Université, Université de Paris, 75005 Paris, France

(Received xx; revised xx; accepted xx)

Vertical thermal convection is a non-equilibrium system in which both buoyancy and shear forces play a role in driving the convective flow. Beyond the onset of convection, the driven dissipative system exhibits chaotic dynamics and turbulence. In a three-dimensional domain extended in both the vertical and the transverse dimensions, [Gao *et al.* \(2018\)](#) have observed a variety of convection patterns which are not described by linear stability analysis. We investigate the fully non-linear dynamics of vertical convection using a dynamical-systems approach based on the Oberbeck–Boussinesq equations. We compute the invariant solutions of these equations and the bifurcations that are responsible for the creation and termination of various branches. We map out a sequence of local bifurcations from the laminar base state, including simultaneous bifurcations involving patterned steady states with different symmetries. This atypical phenomenon of multiple branches simultaneously bifurcating from a single parent branch is explained by the role of D_4 symmetry. In addition, two global bifurcations are identified: first, a homoclinic cycle from modulated transverse rolls and second, a robust heteroclinic cycle linking two symmetry-related diamond-roll patterns. These are confirmed by phase space projections as well as the functional form of the divergence of the period close to the bifurcation points. The intricacy of this bifurcation diagram highlights the essential role played by dynamical systems theory and computation in hydrodynamic configurations.

Key words: Vertical convection, nonlinear dynamical systems, bifurcation theory

1. Introduction

Vertical convection, in which a layer of fluid is confined between two vertical plates maintained at different temperatures, is relevant for industrial applications, including the control of insulation properties of double-glazed windows, but also serves as a model system

† Email address for correspondence: laurette.tuckerman@espci.fr

in the geophysical context to describe convectively driven flows in the earth, the ocean and the atmosphere. Moreover, vertical convection is a fundamental hydrodynamics problem in its own right, allowing to study pattern formation mechanisms within spatially extended driven dissipative nonlinear out-of-equilibrium systems. In our companion paper [Zheng *et al.* \(2024\)](#), we discuss a domain in which only the vertical dimension parallel to gravity was chosen large compared to both the distance between the plates and the transverse (or spanwise) direction, rendering the problem primarily two-dimensional (2D), with variations predominantly in the vertical and wall-normal direction. Here, we will consider a fully three-dimensional (3D) geometry, in which the vertical and the transverse dimensions are both large compared to the inter-plate spacing.

We begin by briefly surveying 3D numerical investigations of vertical convection. [Chait & Korpela \(1989\)](#); [Henry & Buffat \(1998\)](#); [Xin & Le Quéré \(2002\)](#) analyzed the instability of 2D nonlinear flow (transverse rolls) to 3D perturbations in order to determine when and whether the flow could be assumed to be 2D. In Rayleigh-Bénard convection, the stability thresholds in Rayleigh number (Ra), Prandtl number (Pr), and 2D roll wavelength delimit a volume that is called the Busse balloon ([Busse 1978](#)), named after the researcher who has been at the forefront of pattern formation research in Rayleigh-Bénard convection. Busse later also transferred his analysis to vertical convection. In the limit of vanishing Prandtl number, the analysis of convection is simplified, since the diffusive terms dominate in the temperature equation, causing the temperature to retain its laminar state. Thereby, the velocity no longer feeds back on the temperature field and the coupling between velocity and temperature reduces to only one direction. For $Pr = 0$, [Nagata & Busse \(1983\)](#) computed a fully nonlinear 3D solution which is probably the analogue of what we here refer to as the diamond roll state (FP2) to be described in section 3. (Such 3D solutions have sometimes been termed tertiary solutions, while the laminar and 2D transverse roll solutions are called primary and secondary, respectively.) [Clever & Busse \(1995\)](#) extended the computation of 3D solutions to finite Prandtl numbers, more specifically $Pr = 0.71$, corresponding to convection in air, the case we study in this paper.

[Gao *et al.* \(2013, 2015, 2018\)](#) combined linear and weakly non-linear theories as well as direct numerical simulations to study the three-dimensional flow. [Gao *et al.* \(2013, 2015\)](#) studied the equilibria and periodic orbits in a computational domain of size $[L_x, L_y, L_z] = [1, 1, 10]$, the same domain we consider in our companion paper [Zheng *et al.* \(2024\)](#). In order to study secondary instabilities in the transverse direction that two-dimensional steady rolls undergo, [Gao *et al.* \(2018\)](#) computed their linear stability properties. Their analysis showed two types of instabilities, with spanwise wavelengths of about four and eight. They consequently extended the spanwise length of the domain from unity to $L_y = 8$ to capture both instabilities. In addition, when $L_z = 9$ the Rayleigh number thresholds of both types of three-dimensional instabilities are close, motivating them to decrease L_z from 10 to 9 in order to study the competition between both instabilities destabilizing two-dimensional rolls. As for a spanwise domain size of $L_z = 10$, a domain with $L_z = 9$ also accommodates four co-rotating rolls in the primary instability of the base state and is large enough to allow interactions between rolls. [Cimarelli & Angeli \(2017\)](#) and [Cingi *et al.* \(2021\)](#) also investigated configurations similar to those of [Gao *et al.* \(2013, 2018\)](#).

In this paper, we study vertical convection in air ($Pr = 0.71$) in the configuration $[L_x, L_y, L_z] = [1, 8, 9]$. Similarly to the approach described in [Zheng *et al.* \(2024\)](#), we extend the work in [Gao *et al.* \(2018\)](#) by computing the fully non-linear invariant solutions and their bifurcations. This unravels the bifurcation-theoretic origins of complex flows and the connections between them. This approach has been applied to inclined layer convection where fascinating convection patterns were observed experimentally by [Daniels *et al.* \(2000\)](#). Through a numerical bifurcation analysis, [Reetz & Schneider \(2020a\)](#) and [Reetz *et al.* \(2020b\)](#)

identified the invariant solutions underlying most of the patterns and constructed bifurcation diagrams connecting them. These invariant solutions capture key features and dynamics of the observed patterns and these branches reveal the origin of exact solutions.

We have discovered three new branches of steady states, which, together with those seen by [Gao *et al.* \(2018\)](#), brings the number of branches observed thus far to six. Several of these are created simultaneously, despite not being related by symmetry. We have shown that this otherwise non-generic phenomenon is explained by the fact that the group D_4 is contained in the symmetry groups of the parent branches; see [Swift \(1985\)](#); [Knobloch \(1986\)](#); [Chossat & Iooss \(1994\)](#); [Bergeon *et al.* \(2001\)](#); [Reetz *et al.* \(2020b\)](#). Here, D_4 symmetry leads to simultaneous bifurcations to states that are aligned with respect to the transverse and vertical directions, and others which are diagonal with respect to them. Competition between aligned and diagonal states is also seen in two periodic orbits that consist of diagonal excursions from more aligned states.

Most of the steady states and periodic orbits in this system are unstable. Calculating them is nevertheless essential for understanding the origin of stable states and for constructing a bifurcation diagram unifying the solutions to a problem. Another role played by unstable states is as way-stations, near which chaotic or turbulent trajectories spend much of their time. These are believed to form the core structures supporting weakly turbulent dynamics. Among the unstable periodic orbits that may influence trajectories of a fluid-dynamical system, we have discovered that some terminate in homoclinic or heteroclinic cycles and hence are no longer available to the system. Although there have been a number of computations of global bifurcations in hydrodynamic systems ([Tuckerman & Barkley 1988](#); [Prat *et al.* 2002](#); [Nore *et al.* 2003](#); [Millour *et al.* 2003](#); [Abshagen *et al.* 2005](#); [Bordja *et al.* 2010](#); [Bengana & Tuckerman 2019](#); [Reetz *et al.* 2020b](#)), we are not aware of previous calculations of such cycles in vertical convection.

The remainder of this manuscript is organised as follows: in §2 we summarize the key numerical methods used in our research which are already presented in detail in [Zheng *et al.* \(2024\)](#). The results from the bifurcation analysis will be shown in §3 for fixed points and in §4 for periodic orbits. Concluding remarks and future research directions will be outlined in §5.

2. System and methods

We refer readers to [Reetz \(2019\)](#); [Reetz & Schneider \(2020a\)](#); [Reetz *et al.* \(2020b\)](#); [Zheng *et al.* \(2024\)](#) for detailed descriptions of the numerical methods used in the research. Here, we will only summarize the key points.

2.1. Direct numerical simulation of vertical convection

The vertical convection system is studied numerically by performing direct numerical simulations (DNS) with the ILC extension module of the *Channelflow 2.0* code ([Gibson *et al.* 2021](#)), to solve the non-dimensionalized Oberbeck–Boussinesq equations:

$$\frac{\partial \mathbf{u}}{\partial t} + (\mathbf{u} \cdot \nabla) \mathbf{u} = -\nabla p + \left(\frac{Pr}{Ra}\right)^{1/2} \nabla^2 \mathbf{u} + \mathcal{T} \mathbf{e}_z, \quad (2.1a)$$

$$\frac{\partial \mathcal{T}}{\partial t} + (\mathbf{u} \cdot \nabla) \mathcal{T} = \left(\frac{1}{Pr Ra}\right)^{1/2} \nabla^2 \mathcal{T}, \quad (2.1b)$$

$$\nabla \cdot \mathbf{u} = 0, \quad (2.1c)$$

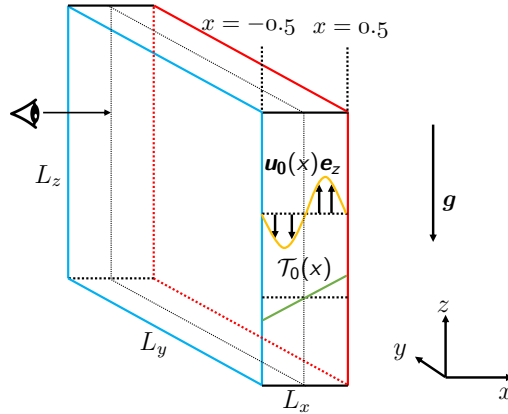


Figure 1: Schematic of the vertical convection cell approximating $[L_x, L_y, L_z] = [1, 8, 9]$. The flow is bounded between two walls in x direction at $x = 0.5$ where the flow is heated and at $x = -0.5$ where the flow is cooled. The domain is periodic in y and z directions. The y - z plane at $x = 0$ (dotted) corresponds to the visualization plane in this paper and all the snapshots presented in this paper are visualized from negative to positive x , as indicated by the eye and arrow. The laminar velocity and temperature are shown as the orange curve and green line, respectively.

with periodic boundary conditions in y and z . The boundary conditions in x at the two walls are of Dirichlet type:

$$\mathbf{u}(x = \pm 0.5) = 0, \quad \mathcal{T}(x = \pm 0.5) = \pm 0.5. \quad (2.2)$$

The laminar solution, illustrated in figure 1, is:

$$\mathbf{u}_0(x) = \frac{1}{6} \sqrt{\frac{Ra}{Pr}} \left(\frac{1}{4}x - x^3 \right) \mathbf{e}_z, \quad (2.3a)$$

$$\mathcal{T}_0(x) = x, \quad (2.3b)$$

$$p_0(x) = \Pi, \quad (2.3c)$$

with arbitrary pressure constant Π .

The governing equations and boundary conditions are discussed in our companion paper [Zheng et al. \(2024\)](#). The only aspect which differs here is the domain size: instead of the narrow domain $[L_x, L_y, L_z] = [1, 1, 10]$ with one extended direction studied in [Gao et al. \(2013\)](#), here we study the three-dimensional computational domain $[L_x, L_y, L_z] = [1, 8, 9]$ of [Gao et al. \(2018\)](#). This domain has two extended directions and is illustrated in figure 1. This domain is spatially discretized by $[N_x, N_y, N_z] = [31, 96, 96]$ Chebychev-Fourier-Fourier modes.

2.2. Symmetries and computation of invariant solutions

We will often refer to the symmetries of our system, the group S_{VC} , which is generated by reflection in y , combined reflection of x , z and \mathcal{T} , and translation in y and z :

$$\pi_y[u, v, w, \mathcal{T}](x, y, z) \equiv [u, -v, w, \mathcal{T}](x, -y, z), \quad (2.4a)$$

$$\pi_{xz}[u, v, w, \mathcal{T}](x, y, z) \equiv [-u, v, -w, -\mathcal{T}](-x, y, -z), \quad (2.4b)$$

$$\tau(\Delta y, \Delta z)[u, v, w, \mathcal{T}](x, y, z) \equiv [u, v, w, \mathcal{T}](x, y + \Delta y, z + \Delta z), \quad (2.4c)$$

stated more compactly as $S_{VC} \equiv \langle \pi_y, \pi_{xz}, \tau(\Delta y, \Delta z) \rangle \simeq [O(2)]_y \times [O(2)]_{x,z}$. The first $O(2)$ refers to the symmetry group in y while the second $O(2)$ refers to the symmetry group

in (x, z) , a convention that we will use in the rest of the paper where possible. Note that the generators of a group are non-unique, as is the decomposition into direct products (indicated by \times). The groups we use are Z_n , the cyclic group of n elements, D_n , the cyclic group of n elements together with a non-commuting reflection, and $O(2)$, the group of all rotations together with a non-commuting reflection. Note that $D_1 = Z_2$ and $D_2 = Z_2 \times Z_2$.

We adopt the shooting-based matrix-free Newton method implemented in *Channelflow 2.0* to compute invariant solutions. The only difference with respect to our description in [Zheng et al. \(2024\)](#) arises from the presence here of homoclinic and heteroclinic orbits. While the Newton method can converge with one shot in most of the cases (provided that the guess is sufficiently close to the solution), the multi-shooting method ([van Veen et al. 2011](#); [Sánchez & Net 2010](#)) is required in order to converge orbits with long periods (typically $T > 300$ in our case) that are close to a global bifurcation point and very unstable orbits. For these periodic orbits, we employ the multi-shooting method with at most six shots.

To characterise the stability of a solution, its leading eigenvalues and eigenvectors for fixed points, or Floquet exponents and Floquet modes for periodic orbits, are determined by Arnoldi iterations. When solutions have symmetries, the resulting linear stability problem has the same symmetries, leading to multiple eigenvectors sharing the same eigenvalues. In such cases, we choose the eigenvectors appropriate to our analysis either by subtracting two nonlinear flow fields along a trajectory or branch, or by imposing symmetries.

2.3. Order parameter and flow visualization

Once an equilibrium or time-periodic solution is converged, parametric continuation in Rayleigh number is performed to construct bifurcation diagrams. Solutions are represented via the L_2 -norm of their temperature deviation $\theta \equiv \mathcal{T} - \mathcal{T}_0$. Branches of fixed points are represented by curves showing $\|\theta\|_2$ as a function of Ra ; for periodic orbits, the maximum and minimum of $\|\theta\|_2$ along an orbit are plotted. The thermal energy input I and viscous dissipation D are used to plot phase portraits.

3. Fixed points

We begin by noting that the numbering used for fixed points and for periodic orbits applies only to this paper; except for FP1, the fixed points and periodic orbits here are not the same as those in [Zheng et al. \(2024\)](#).

3.1. Three known fixed points: FP1-FP3

[Gao et al. \(2018\)](#) observed three fixed points in the domain $[L_x, L_y, L_z] = [1, 8, 9]$ and presented visualisations and Fourier decompositions of them. These states have been recomputed here and their flow structures are shown in figures 2(b-d). In this work, we identify the bifurcations that create and destroy these states and construct a bifurcation diagram that includes stable and unstable branches. As presented in the bifurcation diagram in figure 2(a), the laminar base flow is stable until $Ra = 5707$, where the first fixed point, FP1, bifurcates. As in [Zheng et al. \(2024\)](#), FP1 is called two-dimensional or transverse rolls and it is shown in figure 2(b). [Cingi et al. \(2021\)](#) have reported bistability between the base flow and two-dimensional rolls in several Rayleigh-number ranges, but their interpretation contradicts the results obtained here and also those reported by [Gao et al. \(2018\)](#). In particular, those authors find the laminar flow to be bistable with 2D rolls (FP1) over the Rayleigh number range of $[5708, 7000]$. We believe this reported bistability to be spurious, and to almost certainly result from using a time-stepping code to simulate a weakly unstable state without monitoring the growth or decay of perturbations, i.e. without a complementary linear stability analysis.

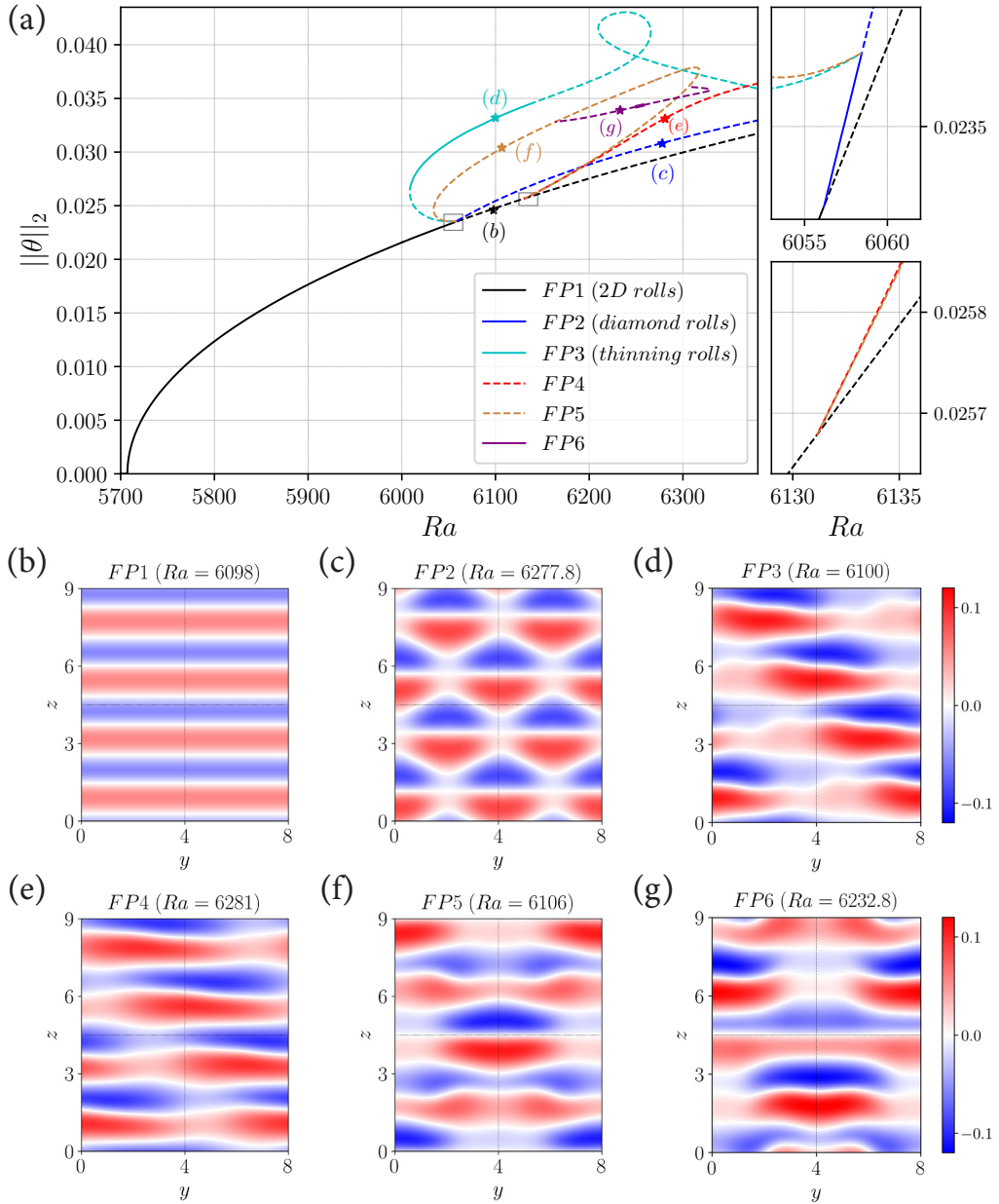


Figure 2: Bifurcation diagram (a) and flow structures visualized via the temperature field on the y - z plane at $x = 0$ (b-g) of six equilibria in domain $[L_x, L_y, L_z] = [1, 8, 9]$. The diagram shows two supercritical pitchfork bifurcations, one from the base state to $FP1$ (b) and another one from $FP2$ (c). $FP3$ (d) bifurcates from $FP2$ in a subcritical pitchfork bifurcation. The unstable $FP4$ (e) bifurcates supercritically from $FP1$. The unstable $FP5$ branch (f) bifurcates at one end subcritically from $FP2$, and at the another end supercritically from $FP1$. $FP3$ and $FP5$ bifurcate together from $FP2$, while $FP4$ and $FP5$ bifurcate together from $FP1$. The two grey rectangles surround these two simultaneous bifurcations, which are also shown in the enlarged diagrams on the right. $FP6$ bifurcates from $FP5$ in two supercritical pitchfork bifurcations and it connects $FP5$ at two Rayleigh numbers. In (a), solid and dashed curves signify stable and unstable states respectively. The ranges over which $FP2$, $FP3$ and $FP6$ are stable are $[6056, 6058.5]$, $[6008.5, 6140]$ and $[6251.4, 6257.6]$, respectively. The stars in (a) indicate the locations of the visualisations of (b-g). $FP1$, $FP2$ and $FP3$ are discussed in [Gao et al. \(2018\)](#) while $FP4$, $FP5$ and $FP6$ are newly identified in this work.

FP1 loses stability at $Ra = 6056$ via a circle pitchfork bifurcation that breaks the y translation symmetry $\tau(\Delta y, 0)$ and creates FP2, shown in figure 2(c). We will refer to these as diamond rolls, while Gao *et al.* (2018) called them wavy rolls. FP2 results from the subharmonic varicose instability of FP1 and this instability is discussed in Subramanian *et al.* (2016); Reetz *et al.* (2020b). FP2 undergoes a subcritical pitchfork bifurcation at $Ra = 6058.5$, so that its stability range is only $[6056, 6058.5]$. The time-dependent simulations of Cingi *et al.* (2021) did not detect FP2. In contrast, Gao *et al.* (2018) observed FP2 as a transient at $Ra = 6100$ and computed its threshold via a linear stability analysis. Clever & Busse (1995) computed a state resembling FP2 by means of a steady-state calculation. (Their threshold of about $Ra \approx 6295$ can perhaps be attributed to a lack of spatial resolution available in 1995.)

The bifurcation from FP2 creates FP3, which Gao *et al.* (2018) call thinning rolls. Initially unstable, FP3 is stabilized by a saddle-node bifurcation at $Ra = 6008.5$. At higher Rayleigh number, FP3 undergoes two additional saddle-node bifurcations at $Ra = 6265.8$ and $Ra = 6209.56$. As pointed out by Gao *et al.* (2018), FP3 can have either of two possible diagonal orientations. Figure 2(d) shows one of the two cases: the slightly wider red portions are located along a diagonal joining the top left with the bottom right.

The symmetry (isotropy) groups of FP1-FP3 are

$$\begin{aligned} \text{FP1: } & \langle \pi_y, \tau(\Delta y, 0), \pi_{xz}, \tau(0, L_z/4) \rangle && \simeq [O(2)]_y \times [D_4]_{xz}; \\ \text{FP2: } & \langle \pi_y, \tau(L_y/2, 0), \pi_{xz}, \tau(L_y/4, L_z/4) \rangle && \simeq [D_2]_y \times D_4; \\ \text{FP3: } & \langle \pi_y \pi_{xz}, \tau(L_y/4, -L_z/4) \rangle && \simeq Z_4. \end{aligned} \quad (3.1)$$

Note that $\tau(L_y/4, -L_z/4) = \tau(L_y/4, 3L_z/4)$, that the reflection in FP3 commutes with the rotations (or translations), and finally that the symmetry groups for FP2 and FP3 cannot be divided into those related to y and those related to x, z .

3.2. Three new fixed points: FP4-FP6

We have also found three new branches of fixed points, FP4-FP6. As shown in figure 2(e), FP4 bifurcates from FP1 in a supercritical pitchfork bifurcation at $Ra = 6131$ and shares with FP3 a diagonal orientation. FP4 also consists of rolls with a slight wavy modulation along the y direction, but this modulation is weaker than that of FP3. FP4 plays an essential role in one of the global bifurcations that we will discuss in §4.1.2.

After bifurcating supercritically from FP1 at $Ra = 6131$, FP5, shown in figure 2(f), undergoes saddle-node bifurcations at $Ra = 6317.5$ and $Ra = 6034$, towards decreasing and increasing Rayleigh number, respectively, and finally terminates at $Ra = 6058.5$ by meeting FP2 in a subcritical pitchfork bifurcation. Thus, FP5 forms a closed loop connecting FP1 and FP2 at two different Rayleigh numbers. Both FP4 and FP5 are unstable along their entire branches.

The last new equilibrium, FP6, shown in figure 2(g) is created from FP5 at $Ra = 6164.3$ in a supercritical pitchfork bifurcation, inheriting the instability of FP5 at the bifurcation point. FP6 becomes stable, but only over a very short range $Ra \in [6251.4, 6257.6]$, indicated by the slight thickening of the branch in figure 2(a). FP6 then undergoes a saddle-node bifurcation at $Ra = 6329$ before terminating at the FP5 branch at $Ra = 6305.8$ in another supercritical pitchfork bifurcation.

The symmetry groups of these states are

$$\begin{aligned} \text{FP4: } & \langle \pi_y \pi_{xz}, \tau(L_y/4, -L_z/4) \rangle && \simeq Z_4; \\ \text{FP5: } & \langle \pi_y, \pi_{xz}, \tau(L_y/2, L_z/2) \rangle && \simeq [Z_2]_y \times [Z_2]_{xz} \times Z_2; \\ \text{FP6: } & \langle \pi_y, \pi_{xz} \tau(L_y/2, 0) \rangle && \simeq [Z_2]_y \times Z_2. \end{aligned} \quad (3.2)$$

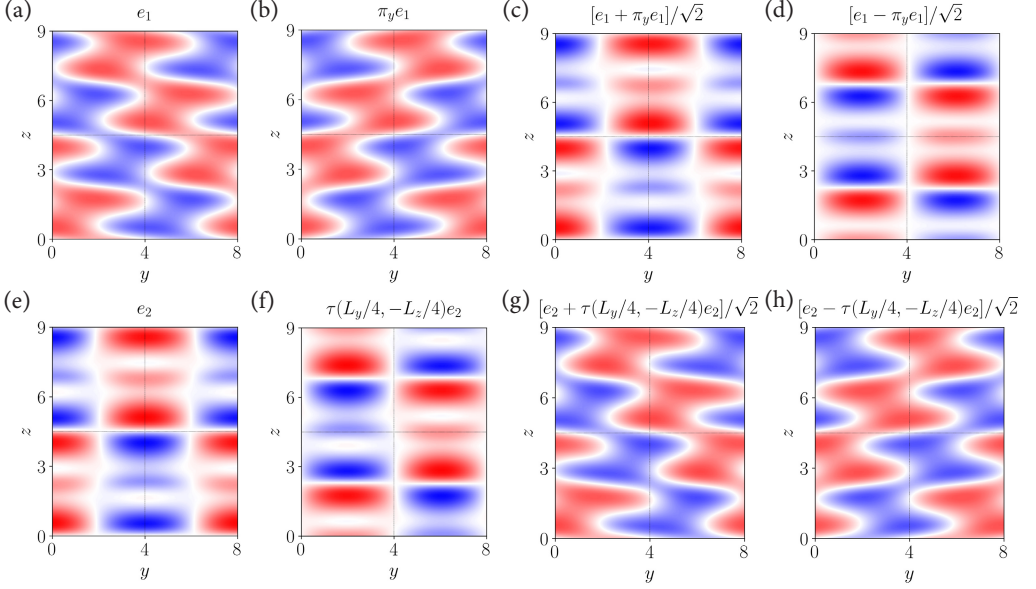


Figure 3: (a) Eigenvector e_1 responsible for FP2→FP3 bifurcation (obtained by subtracting FP2 at $Ra = 6058.5$ from FP3 at $Ra = 6056$) and (b) its y -reflected version $\pi_y e_1$. (c-d) Superpositions $(e_1 \pm \pi_y e_1)/\sqrt{2}$. (e) Eigenvector e_2 responsible for FP2→FP5 bifurcation (obtained by subtracting FP2 at $Ra = 6058.5$ from FP5 at $Ra = 6056$) and (f) its quarter-diagonal translation $\tau(L_y/4, -L_z/4)e_2$. (g-h) Superpositions $(e_2 \pm \tau(L_y/4, -L_z/4)e_2)/\sqrt{2}$. All eigenvectors are visualized via the temperature field on the y - z plane at $x = 0$. The same color bar is used in all plots.

Figure 2 shows clearly that of all these states, only FP1 and FP2 can exist in a smaller domain with $[L_y, L_z] = [4, 4.5]$; states FP3, FP4, FP5, and FP6 all require $[L_y, L_z] = [8, 9]$.

3.3. Two simultaneous bifurcations

The two enlarged bifurcation diagrams on the right of figure 2(a) depict bifurcations at which two qualitatively different branches with different symmetries are created simultaneously. FP3 and FP5 bifurcate simultaneously from FP2 at $Ra = 6058.5$, and FP4 and FP5 bifurcate simultaneously from FP1 at $Ra = 6131$. These simultaneous bifurcations can be explained by the same D_4 scenario that is discussed in detail in Zheng *et al.* (2024). We repeat here the normal form corresponding to bifurcation in the presence of D_4 symmetry:

$$\dot{p} = (\mu - ap^2 - bq^2)p, \quad (3.3a)$$

$$\dot{q} = (\mu - bp^2 - aq^2)q. \quad (3.3b)$$

The dynamical system (3.3) has the non-trivial solutions

$$p = \pm\sqrt{\mu/a} \quad q = 0, \quad (3.4a)$$

$$p = 0 \quad q = \pm\sqrt{\mu/a}, \quad (3.4b)$$

$$p = \pm\sqrt{\mu/(a+b)} \quad q = \pm\sqrt{\mu/(a+b)}, \quad (3.4c)$$

$$p = \pm\sqrt{\mu/(a+b)} \quad q = \mp\sqrt{\mu/(a+b)}, \quad (3.4d)$$

i.e. two classes of solutions, (3.4a)-(3.4b), which we call here the diagonal solutions, and (3.4c)-(3.4d), which we call here the rectangular solutions, for reasons which figure 3 will

make clear. The diagonal solutions are related to one another by symmetry, as are the rectangular ones, but the diagonal solutions are not related by symmetry to the rectangular solutions.

We begin by explaining the simultaneous bifurcation from FP2. The symmetry group D_4 of FP2 is generated by the translation operator $\tau(L_y/4, -L_z/4)$ together with either of the reflection operators, π_y or π_{xz} . FP2 is invariant under any product of these operations. In the model (3.3), FP2 corresponds to the trivial solution $p = q = 0$ from which the other solutions bifurcate.

When FP2 loses stability at $Ra = 6058.5$, a real eigenvalue $\lambda_{1,2}$ crosses the imaginary axis. This double eigenvalue has a two-dimensional eigenspace, spanned by any two of its linearly independent eigenvectors. Figure 3(a) shows the eigenvector e_1 of FP2 giving rise to state FP3 shown in figure 2(d), while figure 3(b) shows its y -reflection, $\pi_y e_1$. Since π_y belongs to the symmetry group of FP2, $\pi_y e_1$ is also an eigenvector of FP2, as is any superposition of e_1 and $\pi_y e_1$. The diagonal solution (3.4a) represents FP3 which arises from eigenvector e_1 . Solution (3.4b) represents $FP3' \equiv \pi_y FP3$, whose diagonal is reversed and which arises from eigenvector $\pi_y e_1$. The amplitudes of e_1 and $\pi_y e_1$ are represented in the model (3.3) by variables p and q :

$$FP3 = FP2 + p(t)e_1 + q(t)\pi_y e_1. \quad (3.5)$$

The eigenvector e_2 of FP2 leading to state FP5 is shown in figure 3(e). Eigenvector e_2 turns out to be identical to the equal superposition of e_1 and $\pi_y e_1$, as shown in figure 3(c). This is a manifestation of the fact that, in the model (3.3), the rectangular solutions (3.4c) and (3.4d) contain equal amplitudes of p and q . The shifted eigenvector $\tau(L_y/4, -L_z/4)e_2$ leads to $FP5' \equiv \tau(L_y/4, -L_z/4)FP5$; its superposition with e_2 produces e_1 . Indeed, in the model (3.3), equal superpositions of rectangular solutions of types (3.4c) and (3.4d) produce the diagonal solutions of types (3.4a) and (3.4b). (Figures 3(d) and (h) are also eigenvectors of FP2, identical to figures 3(f) and (b), respectively.) In figure 3, the eigenvectors have been approximated by subtracting FP2 from FP3 and from FP5 just beyond the bifurcation point ($Ra = 6058.5$ for FP2 and $Ra = 6056$ for FP3 and FP5). This selects the appropriate choices out of the multitude of eigenvectors of the highly symmetric FP2.

Just as solutions (3.4c) and (3.4d) are not related to solutions (3.4a) or (3.4b) by any symmetry operation, FP5 cannot be produced by a symmetry transformation from FP3. In addition, figure 2 makes it clear that branches FP3 and FP5 behave differently, with a different global temperature norm and different saddle-node bifurcations.

We turn now to the simultaneous bifurcations of FP4 and FP5 from FP1 at $Ra = 6131$. The symmetries of FP1 are generated by reflection and translation in y together with reflection in (x, z) and four-fold-translation in z , i.e. $[O(2)]_y \times [D_4]_{xz}$. We again compute the eigenvectors of FP1 responsible for these two bifurcations. Taking symmetry transformations and superpositions, we obtain the eigenvector responsible for FP5 (FP4) as the equal superposition of the eigenvector responsible for FP4 (FP5) with a symmetry-transformed version of it.

Interestingly, the eigenvectors responsible for the simultaneous bifurcation from $FP1 \rightarrow (FP4, FP5)$ at $Ra = 6131$ are very similar to those responsible for the simultaneous bifurcation from $FP2 \rightarrow (FP3, FP5)$ at $Ra = 6058.5$. This can be explained as follows. The two simultaneous bifurcations occur at Rayleigh numbers which are close to each other and to $Ra = 6056$, at which FP2 is formed via a supercritical circle pitchfork bifurcation from FP1. FP2 inherits the spectrum of FP1, with the exception of the double eigenvalue responsible for the circle pitchfork. (Just above $Ra = 6056$, this double eigenvalue becomes positive for FP1, whereas it splits into a zero and negative eigenvalue for FP2.) The other eigenvectors and eigenvalues of FP2 at $Ra = 6058.5$ are close to those of FP1 at $Ra = 6131$,

including those shown in figure 3 which cause the simultaneous bifurcations. We do not show the eigenvectors of FP1 to avoid repetition.

It has been known since the mid-1980s (Swift 1985) that D_4 symmetry leads to the simultaneous creation of non-symmetry-related branches. This has been applied to a number of situations, such as the simultaneous creation of standing and traveling waves (Knobloch 1986; Borońska & Tuckerman 2006; Reetz *et al.* 2020b). The application most relevant here is that of counter-rotating Taylor-Couette flow, in which spirals were first described in the classic paper by Taylor (1923). The superposition of spirals of opposite helicity leads to a state called ribbons, much as the superposition of diagonal states produces the rectangular states in the current study. Exceptionally, ribbons were first predicted mathematically (Demay & Iooss 1984; Chossat & Iooss 1994), setting off a quest to observe them experimentally, which was finally achieved by Tagg *et al.* (1989).

4. Periodic orbits

In this section, we explore four periodic orbits, PO1 to PO4. Periodic orbits PO1 to PO3 are created by a sequence of local bifurcations (i.e. bifurcations associated with a change in the real part of one or more eigenvalues/Floquet exponents): $FP3 \rightarrow PO1 \rightarrow PO2 \rightarrow PO3$. PO1 and PO2 disappear in a global homoclinic and heteroclinic bifurcation, respectively, while the termination of PO3 is not discussed in this work. PO4 bifurcates from and terminates on FP6 via Hopf bifurcations. The bifurcation diagram of figure 4(a) shows the six equilibria discussed in §3 and the four periodic orbits to be discussed, while the periods of the limit cycles are shown in figure 4(b).

4.1. First periodic orbit (PO1)

4.1.1. Creation of PO1: Hopf bifurcation

Produced by a subcritical pitchfork bifurcation from FP2, FP3 is unstable at onset, but is stabilized by a saddle-node bifurcation at $Ra = 6008.5$ and then loses stability again at $Ra = 6140$ via a Hopf bifurcation that produces a periodic orbit PO1. The S-shaped green curve in figure 4(a) contains the maximum (above the cyan curve of FP3) and minimum (below the cyan curve) values of $\|\theta\|_2$ over the period of each PO1 state. The period (T) of PO1 increases smoothly before the saddle-node bifurcation at $Ra = 6157.97$. PO1 loses stability before the fold by undergoing a period-doubling bifurcation at $Ra = 6154.7$ to PO2, which will be discussed in §4.2.1. The new branch produced by the saddle-node bifurcation can be seen in both the maximum and minimum dashed green curves of figure 4(a); in the following, we call it the lower branch because the $\|\theta\|_2$ of this new branch is lower than that of the old branch.

By using the multi-shooting method with two to five shots, we have been able to continue the lower PO1 branch down in Rayleigh number to $Ra = 6152.2041$, where the period of PO1 is very long: $T = 955.4$ time units. We will see below that PO1 disappears via a homoclinic bifurcation, at which its period is infinite. Figures 5(a)-(d) show snapshots of PO1 at $Ra = 6152.249$, on the lower branch. Among these snapshots, (a) and (b) capture the thinning and thickening of the rolls along the diagonal, with local waviness along the edge of the rolls. The waviness becomes weaker in (c) and finally in (d) the edges are smoother and the roll widths almost uniform. All of the states in the cycle have a definite diagonal orientation. This implies that there exists another version of PO1 with the opposite diagonal orientation. The times at which these snapshots are taken are marked by stars in figures 5(e-f).

Figure 5(e) shows time series initialized with this unstable PO1 and also with FP4 (with

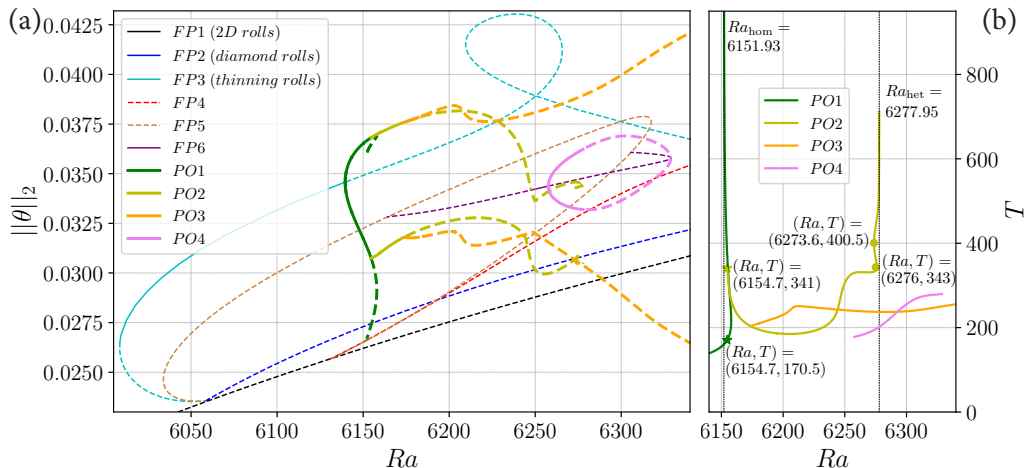


Figure 4: (a) Bifurcation diagram of fixed points (FPs) and periodic orbits (POs) and (b) periods of four periodic orbits in domain $[L_x, L_y, L_z] = [1, 8, 9]$. In (a), for each periodic orbit, we show two curves, the maximum and minimum of $\|\theta\|_2$ along an orbit. PO1 bifurcates from FP3 at $Ra = 6140$ and undergoes a period-doubling bifurcation at $Ra = 6154.7$ giving rise to PO2. PO1 then undergoes a saddle-node bifurcation at $Ra = 6157.97$ and disappears by meeting FP4 in a homoclinic bifurcation at $Ra_{\text{hom}} = 6151.93$ at which its period diverges; see (b). PO2 loses stability at $Ra = 6173.8$ where PO3 is created via a supercritical pitchfork bifurcation. The stability of PO2 changes multiple times along the branch for $6235 < Ra < 6255$, see details in figure 8. PO2 then undergoes two saddle-node bifurcations before terminating by meeting two symmetrically-related versions of FP2 in a heteroclinic bifurcation at $Ra_{\text{het}} = 6277.95$, at which its period diverges. PO3 is continued until $Ra = 6407.3$ (the range $6340 < Ra < 6407.3$ is not shown) and its period remains approximately constant. The apparent lack of smoothness in the curves representing PO2 and PO3 (in (a) around $Ra = 6250$) corresponds to the overtaking of one temporal maximum or minimum of $\|\theta\|_2$ by another as Ra is varied. PO4 bifurcates from and terminates on FP6 at $Ra = 6257.6$ and $Ra = 6328.8$, and it is stable within $6257.6 < Ra < 6278$. In (a), solid and dashed curves signify stable and unstable states respectively, and the curves representing periodic orbits are slightly thicker than those of fixed points. The same color code is used in (a) and (b).

a small perturbation), at $Ra = 6152.249$. Both of these runs eventually converge to another state: the stable upper branch of PO1, whose period $T = 161$ is much shorter than the period $T = 900$ of the lower branch PO1. For $t < 1000$, the red curve remains close to FP4 during a large portion of the period. Figure 5(d) corresponds to the fourth star of 5(e), indicating via this projection that (d) is long-lived and very close to FP4. Indeed we used figure 5(d) as the initial estimate for Newton's method to converge to FP4 at $Ra = 6152.249$. However, figure 5(c), which only shows a transient at $Ra = 6152.249$, resembles figure 2(e), which shows the converged FP4 at $Ra = 6281$. We see from this that the diagonal orientation of FP4 becomes more prominent at higher Rayleigh numbers. Figure 5(f) shows a phase portrait visualization of the same data as (e). There, FP4 is shown as the hollow blue circle on the $D/I = 1$ vertical line, showing that energy dissipation and input are equal. Near FP4, the dotted red curve looks continuous; this is due to the clustering of points near FP4.

4.1.2. Termination of PO1: homoclinic bifurcation

The close approach to FP4 implies that PO1 is close to a homoclinic cycle. We have verified that this closest approach is always to the same version of FP4 and not to another symmetry-related version. Thus, PO1 approaches a homoclinic, and not a heteroclinic cycle. A homoclinic cycle approaches a fixed point along one of its stable directions and escapes from it along one of its unstable directions. For this reason, we compute the eigenvalues and eigenvectors of FP4. Figure 6(a) shows the leading eigenvalues that we have computed

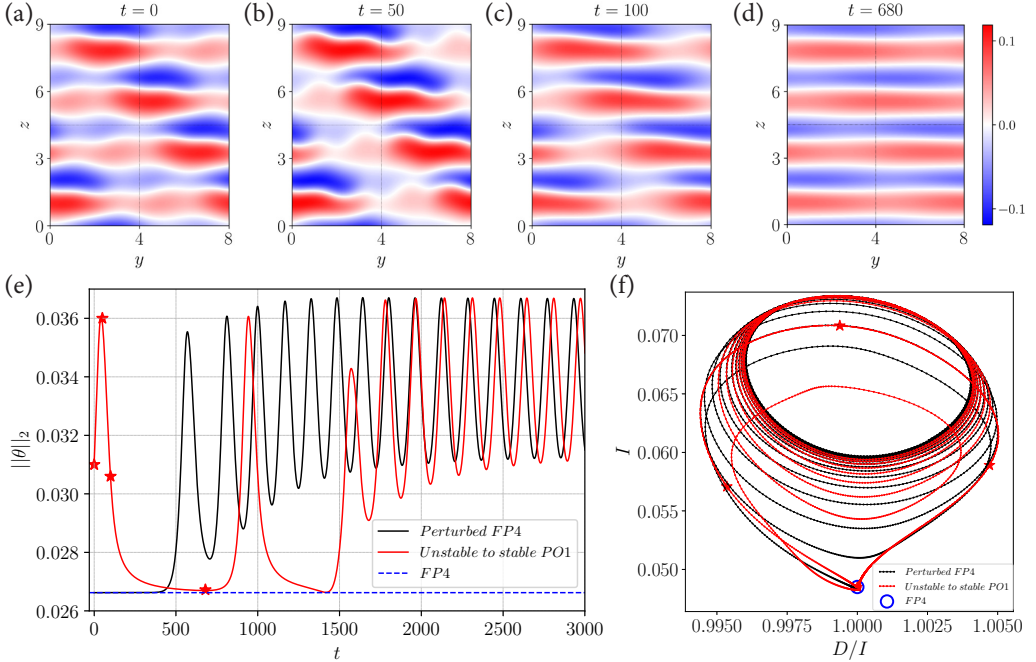


Figure 5: (a-d) The dynamics of PO1 (visualized via the temperature field on the y - z plane at $x = 0$) on the unstable lower branch at $Ra = 6152.249$ ($Ra_{\text{hom}} = 6151.93$). Snapshot (d) converges to FP4 when used as an initial estimate for Newton solving. (e) Time series from DNS at $Ra = 6152.249$ ($T = 900$), initialized by the unstable PO1 shown in (a) (red curve) and by FP4 with a small perturbation (black). The trajectory initialized by the unstable PO1 spends a long time near FP4 ($250 < t < 800$). Both simulations converge to the stable PO1 branch ($t > 2500$) at this Rayleigh number. (f) Phase portrait illustrating the same data set as in (e). The plot shows the thermal energy input (I) versus the viscous dissipation over energy input (D/I). FP4 (hollow blue circle) is located on the vertical line $D/I = 1$, where energy dissipation and input are equal. The four red stars in (e) and (f) indicate the moments at which the snapshots (a)-(d) are taken. The same color code is used in (e) and (f).

at $Ra = 6152.249$, close to the global bifurcation point. The seven leading eigenvalues, all real, are $[\lambda_1, \lambda_2, \lambda_3, \lambda_4, \lambda_5, \lambda_6, \lambda_7] = [0.0212, 0.0208, 0.0026, 0, 0, -0.00017, -0.0034]$. We have set any eigenvalue whose absolute value is less than 10^{-7} to zero. Figure 6(a) shows other eigenvalues with smaller real parts as well and some of the eigenvalues are too close together to be distinguished. Certain eigenvalues of special significance are highlighted by colored circles and their corresponding eigenvectors are shown in figures 6(c-f).

The eigenvectors can be interpreted by considering FP4 and PO1, as depicted in figures 5(a-d). There are two neutral directions, due to the continuous translation symmetry in the periodic directions. Eigenvalue λ_4 is zero and the corresponding eigenvector e_4 , depicted in figure 6(d), is the neutral mode associated with z -translation (i.e. the z derivative) of the roll-like FP4, very close to what is depicted in figure 5(d). There must also be a marginal eigenvector corresponding to y -translation and indeed, $\lambda_5 = 0$ and we have verified numerically that e_5 , depicted in figure 6(e), is the y derivative of FP4. This is not immediately obvious, but note that for z constant, the y derivative of FP4 oscillates in sign and its maxima and minima are located along a diagonal. The green circle in figure 6(a) contains λ_4 and λ_5 (but also λ_6 , whose decay rate is very small).

The other two eigenvectors shown in figures 6(c) and (f) are responsible for the approach to and escape from FP4. We have determined which eigenvalues are associated with approach and escape by comparing them with the observed approach and escape rates, and also

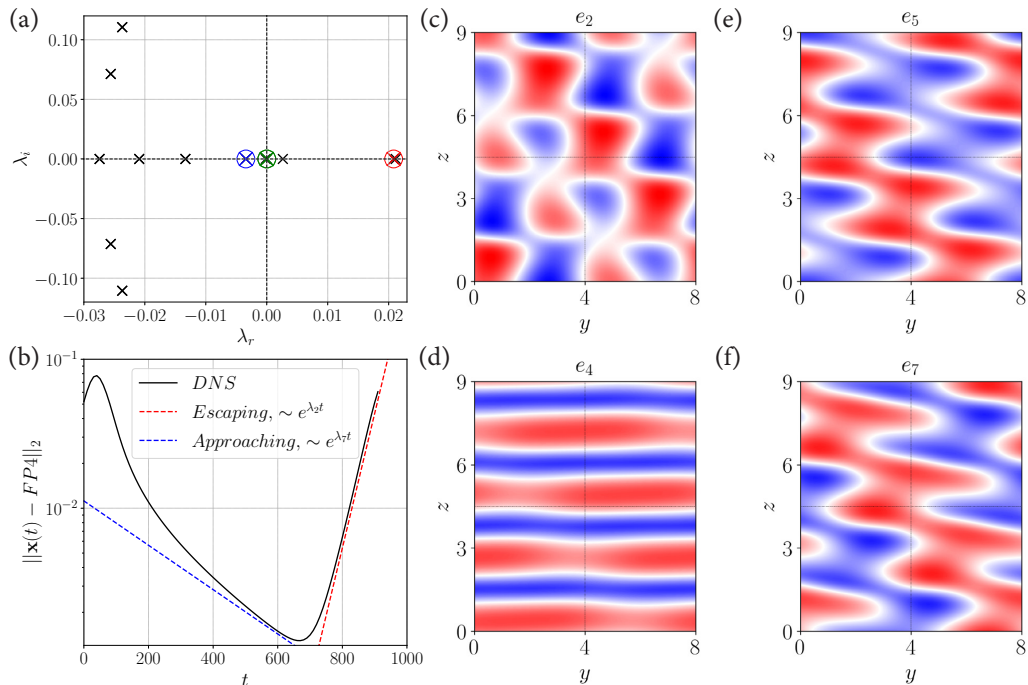


Figure 6: (a) Leading eigenvalues at $Ra = 6152.249$ of FP4: $[\lambda_1, \lambda_2, \lambda_3, \lambda_4, \lambda_5, \lambda_6, \lambda_7] = [0.0212, 0.0208, 0.0026, 0, 0, -0.00017, -0.0034]$. Eigenvalues λ_2 (escaping, red), $\lambda_{4,5}$ (neutral, green) and λ_7 (approaching, blue) are marked in color. (b) L_2 -distance between each instantaneous flow field of PO1 and FP4 at $Ra = 6152.249$, close to $Ra_{\text{hom}} = 6151.93$. The evolution of PO1 (black curve) is exponential most of the time, with the escape from (red line) and approach to (blue line) FP4 governed by λ_2 and λ_7 . (c-f) Four leading eigenmodes of FP4 at $Ra = 6152.249$, visualized via the temperature field on the y - z plane at $x = 0$: e_2 , e_4 , e_5 and e_7 . Same color bar is used in all plots.

by subtracting FP4 from the instantaneous flow fields and comparing the result to the eigenvectors. For the escaping dynamics of PO1 from FP4, the quantity ($\|\mathbf{x}(t) - \text{FP4}\|_2$) increases exponentially at rate $\lambda_2 = 0.0208$. The corresponding eigenvector e_2 is shown in figure 6(c) and can be viewed as corresponding to widening and narrowing of the rolls. The approaching dynamics is characterized by $\lambda_7 = -0.0034$. The corresponding eigenvector e_7 , shown in figure 6(f), can be viewed as corresponding to translation in y . The portion of PO1 escaping FP4 along e_2 can be seen as the red line in figure 6(b); the escaping portion is fit to the red line. While the rate of escape matches λ_2 closely, the approach rate only fits λ_7 over a short range of time. In figure 6(a), the red circle contains λ_2 (but also λ_1 , which is very close to λ_2), while the blue circle encloses λ_7 . Since $|\lambda_2| > |\lambda_7|$, the homoclinic cycle is unstable, as is already seen in the time series in figure 5(e). In addition, a homoclinic orbit bifurcating from a hyperbolic fixed point (which is the case for FP4) is structurally unstable; see Kuznetsov (2004, Lemma 6.1) for a proof. Thus, the homoclinic cycle on which PO1 terminates is neither stable nor robust.

The closeness of some of the eigenvalues in figure 6(a) can be explained by the fact that the y dependence of FP4 is extremely weak. If FP4 were entirely y -independent, like FP1, then eigenvectors would come in pairs, corresponding to a trigonometric dependence (analogous to sine- and cosine-eigenmodes) in y with different phases, or to the choice of diagonal direction. Since the dependence in y is weak, this is still approximately true in many cases. Eigenvalue $\lambda_1 = 0.0212$ is very close to $\lambda_2 = 0.0208$ and indeed eigenvector e_1

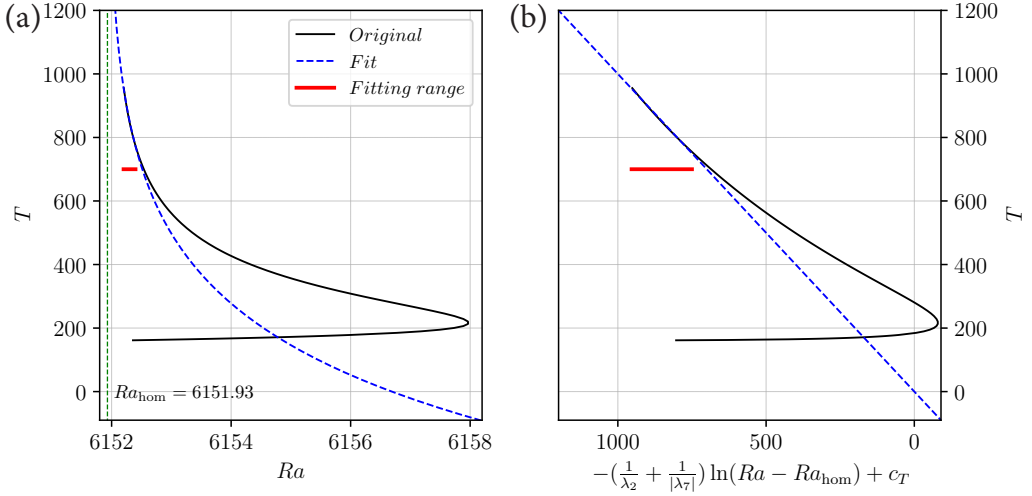


Figure 7: Growth of the period of PO1 close to the global bifurcation point. PO1 undergoes a saddle-node bifurcation at $Ra = 6157.97$ where the lower branch appears. (a) shows the periods computed by numerical continuation and its logarithmic fit (see text). (b) uses a logarithmic scale for $Ra - Ra_{\text{hom}}$, on which the period depends linearly. The red horizontal bar in (a) and (b) indicates the Rayleigh number range $6152.2 < Ra < 6152.4$ used for curve fitting.

(not shown) resembles a y -shifted version of e_2 . The near-neutral eigenvalues $\lambda_3 = 0.0026$ and $\lambda_6 = -0.00017$ correspond to eigenvectors (not shown) which resemble e_5 and e_7 but oriented in the opposite diagonal direction or, equivalently, reflected.

As Ra approaches Ra_{hom} , PO1 approaches FP4 and the time spent near FP4 increases, until PO1 touches FP4 and acquires an infinite period in a homoclinic bifurcation. The period of PO1 is dominated by the time of approach to and escape from FP4, as shown in figure 6(b). This time can be estimated by the formula

$$\begin{aligned}
 T \approx T_+ + T_- &= \frac{1}{\lambda_+} \ln \left[\frac{d_{\text{max}+}}{d_{\text{min}}} \right] + \frac{1}{|\lambda_-|} \ln \left[\frac{d_{\text{max}-}}{d_{\text{min}}} \right] \\
 &= \left(\frac{1}{\lambda_+} + \frac{1}{|\lambda_-|} \right) |\ln |Ra - Ra_{\text{hom}}|| + \underbrace{\left[\frac{1}{\lambda_+} \ln \frac{d_{\text{max}+}}{\alpha} + \frac{1}{|\lambda_-|} \ln \frac{d_{\text{max}-}}{\alpha} \right]}_{c_T}. \quad (4.1)
 \end{aligned}$$

In (4.1), λ_+ and λ_- are the rates of exponential escape from and approach to FP4. The distance of closest approach of PO1 to FP4 is d_{min} . During the escape phase, the distance of PO1 from FP4 increases exponentially from d_{min} to some distance $d_{\text{max}+}$, which takes a time T_+ . During the approaching phase, the distance of PO1 from FP4 decreases exponentially from some distance $d_{\text{max}-}$ to d_{min} , taking a time T_- . The distances $d_{\text{max}\pm}$ vary little with Ra , but the closest distance d_{min} approaches zero like $\alpha |Ra - Ra_{\text{hom}}|$. As shown in figure 7, we have fit the numerically computed periods of the states on the lower branch to the formula (4.1) where $\lambda_+ = \lambda_2 = 0.0208$, $\lambda_- = \lambda_7 = -0.0034$, $Ra_{\text{hom}} = 6151.93$ and $c_T = 520$ is a fitting constant. Note that only the Rayleigh number range $6152.2 < Ra < 6152.4$ very close to Ra_{hom} has been used for fitting and that we have extended the backward continuation of PO1 to the lowest Rayleigh number possible ($Ra = 6152.2041$) within our numerical precision and ability. This asymptotic scaling law for T as a function of Ra has also been discussed and used in Meca *et al.* (2004); Reetz *et al.* (2020b). However they used only one dominant λ , either that of the approach or the escape.

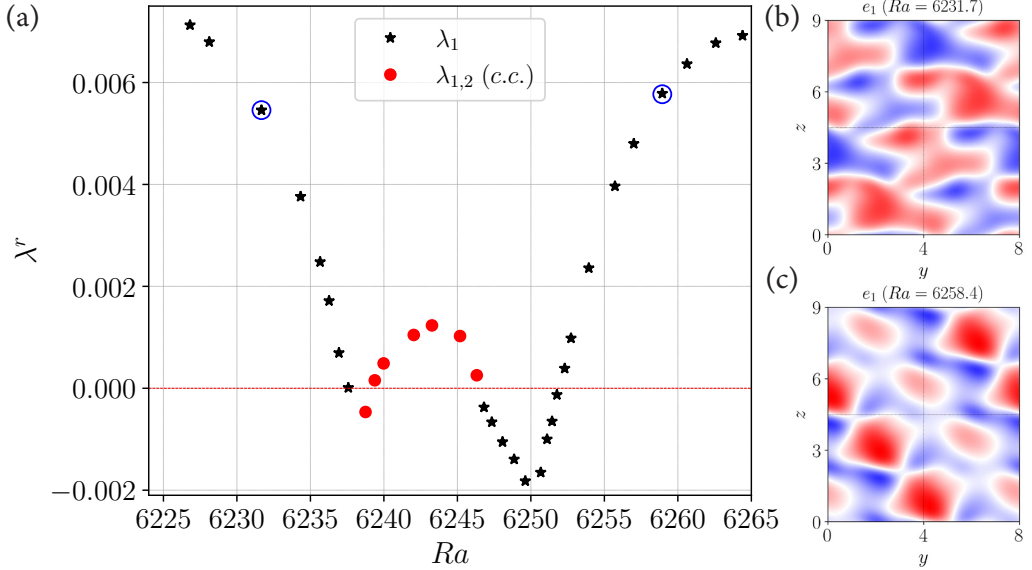


Figure 8: (a) The real part of the leading Floquet exponents of PO2 as a function of Rayleigh number. From low to high Rayleigh number, the leading Floquet exponent decreases monotonically within $6226 < Ra < 6238.75$. At $Ra = 6238.75$, one sees the formation of a complex conjugate pair which has a positive real part for $6239 < Ra < 6246.32$. For $6246.5 < Ra < 6252$, PO2 is stable, with stability lost for $Ra > 6252$. The apparent non-smoothness of the curve at $(Ra, \lambda_1) \approx (6238.7, -0.00047)$ and $(6250, -0.002)$ is due to the crossover of competing leading Floquet exponents. The two blue circles indicate where (b) and (c) are taken. (b-c) Two leading unstable Floquet eigenmodes for $6226 < Ra < 6237.6$ (b) and for $Ra > 6252$ (c), visualized via the temperature field on the y - z plane at $x = 0$. Same color bar is used in (b) and (c).

Gao *et al.* (2018) observed a periodic orbit produced by a Hopf bifurcation from a steady state; these are the solutions that we have called PO1 and FP3. Our bifurcation analysis agrees with their results. Extending their work, we have found that PO1 undergoes a saddle-node bifurcation and then terminates in a homoclinic bifurcation by meeting a new unstable fixed point, FP4.

4.2. Second periodic orbit (PO2)

4.2.1. Creation of PO2: period-doubling bifurcation and restabilisation

PO2 bifurcates from PO1 in a period-doubling bifurcation that was observed by Gao *et al.* (2018) at $Ra = 6250$. We have converged PO2 at $Ra = 6250$ and have continued it down in Rayleigh number to 6154.7, where its period ($T = 341$) is exactly twice that of PO1 ($T = 170.5$), as shown in figure 4(b). We have confirmed the threshold in two additional ways: at $Ra = 6154.7$, the maxima and minima of $\|\theta\|_2$ of PO2 in the time series are extremely close in amplitude and frequency to those of PO1 and the power spectrum contains a very small component of the new frequency of PO2. When increasing Ra from the bifurcation point, the period of PO2 decreases significantly until $Ra = 6204.8$ and then increases until $Ra = 6277.88$ (the last point that we computed along this branch). PO2 undergoes two saddle-node bifurcations at $Ra = 6276$ and then at $Ra = 6273.65$ before disappearing in a global bifurcation, as can be seen in figure 4(b).

PO2 is stable from its onset at $Ra = 6154.7$ until $Ra = 6173.8$, where it becomes unstable via a pitchfork bifurcation that creates another periodic orbit (PO3, discussed in the next subsection). However its observation by Gao *et al.* (2018) via DNS (in their figure 19(a)) implies that PO2 is stable at $Ra = 6250$. The intriguing evolution of the stability of PO2 is

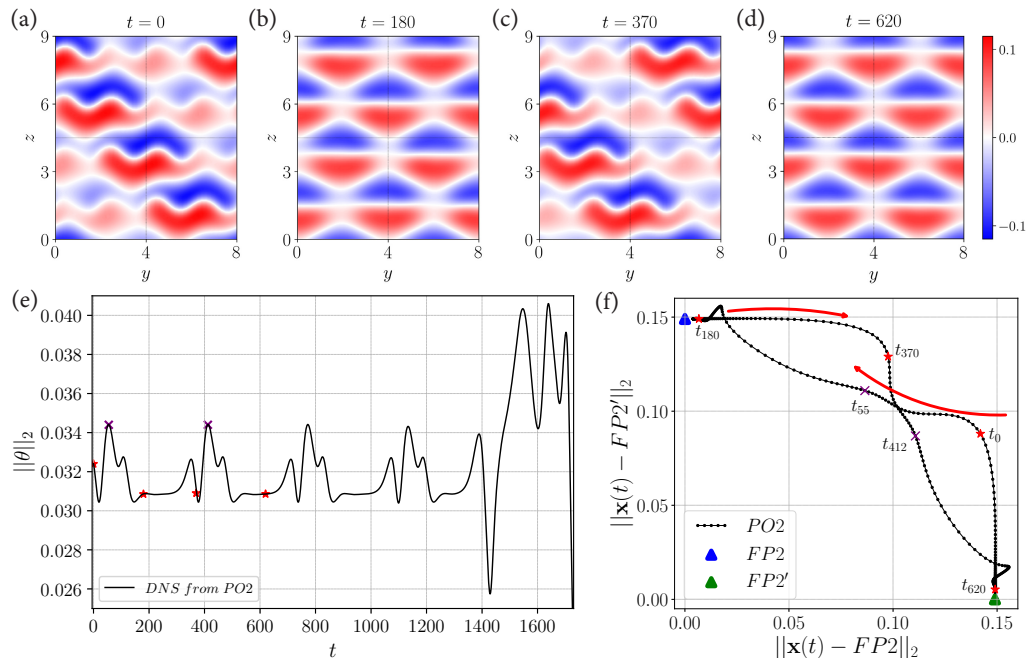


Figure 9: (a-d) Snapshots of the dynamics of PO2 (visualized via the temperature field on the y - z plane at $x = 0$) at $Ra = 6277.88$ near $Ra_{\text{het}} = 6277.95$. Snapshots (b) and (d) show states which are close to two symmetry-related versions of FP2 (figure 2(c)). (e) Time series from DNS at $Ra = 6277.88$, initialized by the unstable PO2 shown in (a). The dynamics after $t \approx 1250$ becomes irregular and eventually terminates in chaos. (f) Phase space projection close to the global bifurcation point: shown are the PO2 at $Ra = 6277.88$ and two symmetry-related FP2 states involved in the heteroclinic cycle. In (e) and (f), the four red stars indicate the moments where the snapshots (a)-(d) are taken and the two purple crosses mark the instants t_{55} and t_{412} . In (f), the red arrows show the direction of the trajectory.

presented in figure 8. The leading Floquet exponent λ_1 of PO2 is real from $Ra = 6173.8$ to $Ra = 6237.6$: it increases monotonically from $Ra = 6173.8$ to $Ra = 6225$ (not shown), and then decreases monotonically to zero over the interval $6226 < Ra < 6237.6$. The leading real exponent is then superseded by a complex conjugate pair $\lambda_{1,2}$ whose real part, initially negative, becomes positive over the interval $6239 < Ra < 6246.32$. The leading exponent λ_1 is then real and negative, so that there is a small interval $6246.5 < Ra < 6252$ over which PO2 is stable. It is within this very short interval that PO2 was observed by Gao *et al.* (2018). In an effort to understand the stabilization and subsequent destabilization of PO2 in this region, we computed the Floquet eigenmode to the left (figure 8(b)) and right (figure 8(c)) of the stable region, but we were unsuccessful in gleaning any physical insight from these. There necessarily exist new branches bifurcating at the values at which λ_1 or the real part of $\lambda_{1,2}$ cross zero, but finding and following these new branches are beyond the scope of the current work.

4.2.2. Termination of PO2: heteroclinic bifurcation

Figures 9(a-d) show four snapshots of the temperature field on the y - z plane of PO2 at $Ra = 6277.88$, very close to the global bifurcation point. Figures 9(b) and (d) are very similar to two symmetry-related versions of FP2, which we denote by FP2 and FP2'. Between these instants, figures 9(a) and (c) show a wavy modulation of convection rolls along one of the diagonals. Although FP2 itself is y -reflection symmetric (no choice of diagonal), there necessarily exists another version of PO2 in which the modulation occurs along the other

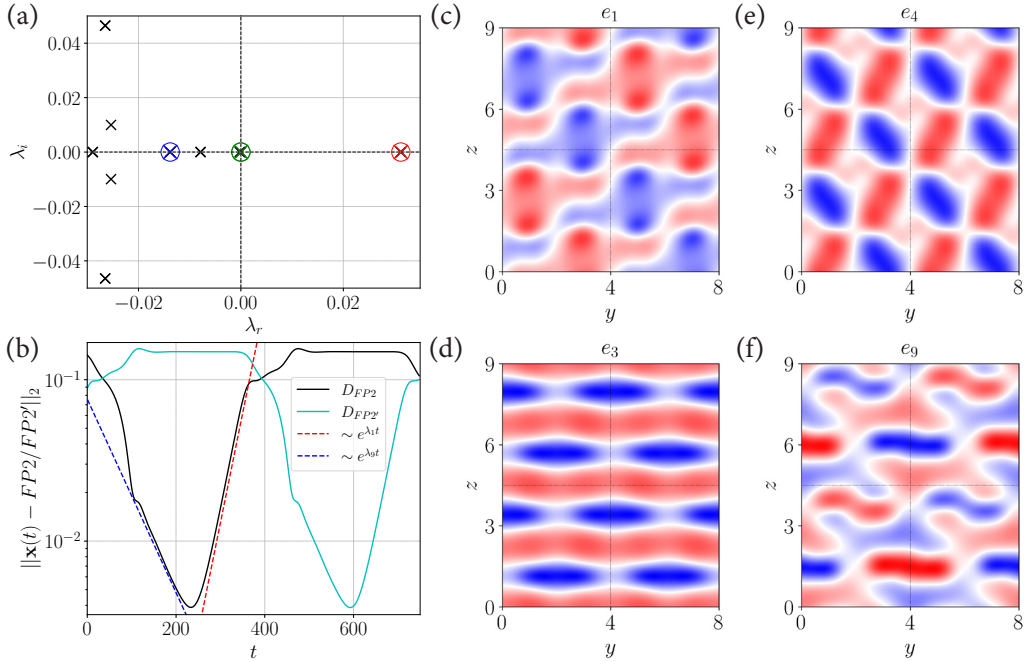


Figure 10: (a) Leading eigenvalues of FP2 at $Ra = 6277.88$. The ten leading eigenvalues are real and double: $[\lambda_{1,2}, \lambda_{3,4}, \lambda_{5,6}, \lambda_{7,8}, \lambda_{9,10}] = [0.031, 0, -0.00019, -0.00788, -0.0138]$. Eigenvalue $\lambda_{1,2}$ (escaping, red), $\lambda_{3,4}$ (neutral, green) and $\lambda_{9,10}$ (approaching, blue) are marked in color. (b) L_2 -distance between each instantaneous flow field of PO2 and FP2 (and FP2') at $Ra = 6277.88$, close to Ra_{het} . The dynamics of PO2 is exponential for most of the cycle (black and cyan curves). The approaching (blue line) and escaping (red line) dynamics of PO2 with respect to FP2 are shown and are governed by two eigenvalues of FP2. (c-f) Four leading eigenmodes of FP2 at $Ra = 6277.88$, visualized via the temperature field on the y - z plane at $x = 0$: e_1 , e_3 , e_4 and e_9 . Same color bar is used in all plots.

diagonal. Figure 9(e) shows a time series of PO2 at $Ra = 6277.88$, indicating the instants at which snapshots in figure 9(a-d) are taken. It is clear that figure 9(b) and (d) belong to fairly long-lived plateaux. The global measurement $\|\theta\|_2$ does not distinguish between FP2 and FP2'. Information complementary to figure 9(e) is given by the phase portrait of figure 9(f), which represents each instantaneous flow field by its distance from FP2 and from FP2'. The phase portrait shows the clustering of points near FP2 and FP2'. All of these features indicate that PO2 is close to a heteroclinic cycle spending long phases near FP2 and FP2'. The phase portrait in figure 9(f) also shows clustering of points around $(0.1, 0.1)$, corresponding to instants t_{38} and t_{394} . This clustering suggests that the limit cycle might be approaching other fixed points. However, the time series in figure 9(e) does not show any other plateaux close to t_{38} and t_{394} , and Newton's method did not converge to any new equilibria around the states from t_{28} to t_{55} and from t_{384} to t_{412} . This remains true up to the highest Rayleigh number (equivalently longest period of PO2) reached by our numerical continuation. We conclude that this heteroclinic cycle visits only two symmetry-related fixed points.

The dynamics along which PO2 approaches and escapes from FP2 can be described by eigenvalues of FP2. Figure 10(a) shows the leading eigenvalues of FP2 at $Ra = 6277.88$, computed by Arnoldi iteration. The leading eigenvalues are $[\lambda_{1,2}, \lambda_{3,4}, \lambda_{5,6}, \lambda_{7,8}, \lambda_{9,10}] = [0.031, 0, -0.00019, -0.00788, -0.0138]$. We previously saw that for FP4, the eigenvalues are approximately double (see figure 6(a)) due to the approximate symmetries of FP4. Here, FP2 has exact reflection symmetries leading to eigenvalues which are exactly double.

The two neutral eigenmodes due to the continuous translation symmetries are e_3 , corresponding to the z derivative of FP2 and shown in figure 10(d) and e_4 , corresponding to its y derivative and shown in figure 10(e). We have verified these by differentiating FP2 in y and z directions. The green circle in figure 10(a) contains $\lambda_{3,4}$, but also $\lambda_{5,6}$. Figure 10(c) shows the escaping eigenmode e_1 , which is responsible for choosing the diagonal orientation of PO2. Looking at figures 9(a-d), this is not obvious, but we have verified that subtracting FP2 from instantaneous temperature fields in the escaping phase of PO2 yields a field resembling e_1 . Moreover, eigenvalues $\lambda_{1,2} = 0.031$ capture well the escape rate from FP2, as shown in figure 10(b). Eigenmode e_2 , with the same eigenvalue, is related to e_1 by reflection symmetry, as shown in figure 3(a)-(b) for $Ra = 6056$. The direction in which PO2 approaches FP2 is e_9 , again confirmed by subtracting FP2 from the appropriate flow field in PO2, and $\lambda_{9,10}$ closely approximate the decay rate to FP2 shown in figure 10(b). Since $|\lambda_{1,2}| > |\lambda_{9,10}|$, the heteroclinic cycle is unstable, which is confirmed by the chaotic behavior in the time series in figure 9(e) after $t \approx 1250$. For FP2, since the eigenvalues are double, the eigenspace corresponding to each is two-dimensional; the eigenvectors that play the roles mentioned above – y -translation, z -translation, escape, and approach – must be selected as linear combinations of the arbitrary two eigenvectors returned by the Arnoldi method. By differentiating FP2 in y and z and by subtracting FP2 from the instantaneous flow fields during approaching or escaping phases, we have been able to choose the appropriate eigenvector in each case.

The heteroclinic cycle discussed above escapes from a fixed point along one of its unstable directions and approaches another symmetry-related fixed point along one of its stable directions. Perturbing FP2 along its unstable eigendirection e_1 gives a half cycle, thus the transition from FP2 to FP2'. Equivalently, perturbing FP2' along its unstable eigendirection $\tau(2, 0)e_1$ triggers the transition back to FP2. A heteroclinic connection is structurally stable if the codimension of the stable manifold (equivalently, the dimension of the unstable manifold) in the symmetry-invariant subspace of the final state FP2' is smaller than or equal to the dimension of the unstable manifold of the initial state FP2, as an intersection between the unstable manifold of the initial state and the stable manifold of the final state is likely to generically exist in a stable way (Halcrow *et al.* 2009). Based on this argument, a heteroclinic connection between two symmetry-related fixed points is likely to be robust. In our heteroclinic cycle, we have confirmed that varying slightly the Rayleigh number does not affect the two transitions of the cycle (FP2→FP2' and FP2'→FP2). Computing the leading eigenvectors of FP2 and of FP2' at surrounding Rayleigh numbers also gives the same or similar unstable modes $e_{1,2}$ (triggering a half cycle), as already shown in figure 10(c). Together, these numerical observations and mathematical arguments suggest that PO2 approaches a heteroclinic cycle which is structurally stable against small perturbations of different parameters.

As depicted in figure 4(b), the period of PO2 increases monotonically for $Ra \geq 6273.6$ and eventually diverges as was discussed for PO1 in §4.1.2. We have been able to continue PO2 until $(Ra, T) = (6277.88, 710.8)$ and the critical Rayleigh number for the heteroclinic bifurcation is estimated to be approximately $Ra_{\text{het}} = 6277.95$.

Gao *et al.* (2018) also reported behavior resembling a nearly heteroclinic cycle in DNS at $Ra = 6250$, where PO2 is stable as discussed in §4.2.1. There, the dynamics passes through the two symmetry-related fixed points (FP2 and FP2'), shown by the later part of the time series in figure 19(a) and by figure 20 in Gao *et al.* (2018). However, since $Ra = 6250$ is still far from the Rayleigh number where the global bifurcation occurs ($Ra \approx 6278$), the dynamics does not stay very long near these two fixed points and the period of PO2 is not yet very long there. This also explains the reason why in the later part of their time series, the plateaux is not obvious to see or long-lived.

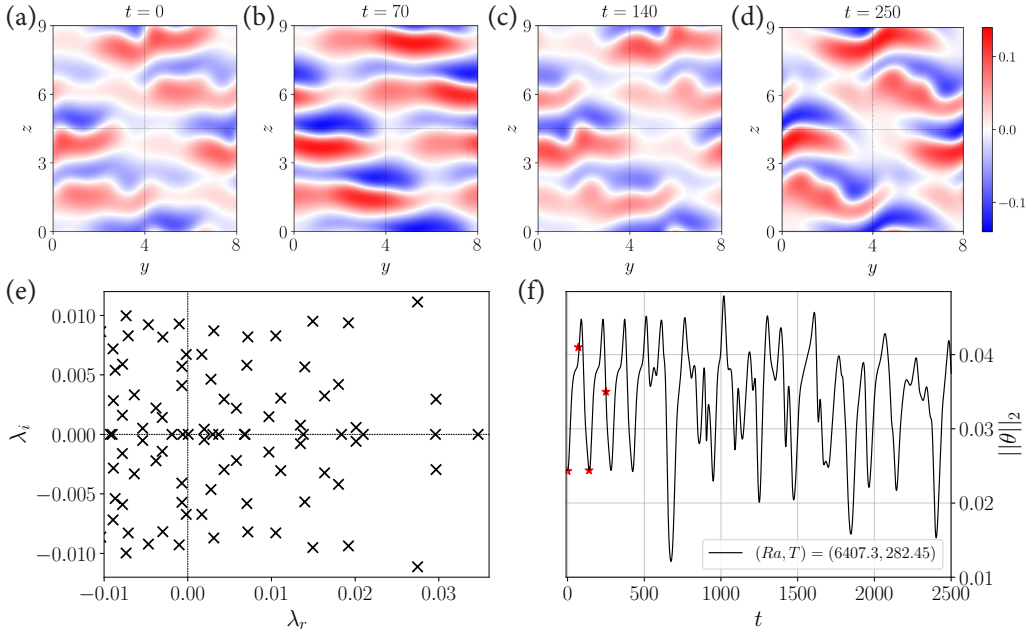


Figure 11: (a-d) Snapshots of the dynamics of PO3 (visualized via the temperature field on the y - z plane at $x = 0$) at $Ra = 6407.3$ showing turbulent and disordered switching rolls. (e) Floquet exponent spectrum of PO3 at $Ra = 6407.3$ showing its 51 unstable Floquet exponents. (f) Time series from DNS at $Ra = 6407.3$, initialized by the converged unstable PO3. The temporal transition from a periodic to chaotic signal occurs at $t \approx 400$. The red stars indicate the moments at which the snapshots (a)-(d) are taken.

4.3. Third periodic orbit (PO3): pitchfork bifurcation

As mentioned in §4.2.1, PO2 loses stability at $Ra = 6173.8$ via a supercritical pitchfork bifurcation which creates a new periodic orbit, PO3. The visual features of PO3 resemble those of PO2 near onset, but become much less regular at higher Rayleigh numbers, for instance at $Ra = 6407.3$, depicted in figures 11(a-d). PO3 loses stability at $Ra = 6183$. The bifurcating Floquet exponent is real, suggesting a pitchfork bifurcation leading to the creation of a new periodic orbit. However, we did not find any stable periodic orbit via DNS in the vicinity of $Ra = 6183$, implying that such a bifurcation would be subcritical. Because PO3 is only stable for $6173.8 \leq Ra \leq 6183$, it is not surprising that it was not observed by Gao *et al.* (2018).

We continued PO3 until $Ra = 6407.3$, considerably into the chaotic regime ($Ra > 6300$) mentioned by Gao *et al.* (2018). (The range $6340 < Ra < 6407.3$ is not included in figure 4.) Parametric continuation of PO3 for $Ra > 6350$ was computationally challenging, probably due to the fact that the orbit is very unstable in this Rayleigh number range; see discussion of the numerical convergence of the iterative Newton algorithm in Sanchez *et al.* (2004) and Reetz *et al.* (2020b). The spectrum of PO3 at $Ra = 6407.3$ has more than 50 unstable eigendirections with a wide range of frequencies, as illustrated in figure 11(e). Moreover, integrating the converged PO3 forward in time at $Ra = 6407.3$, the transition from a periodic to chaotic state is triggered after fewer than two periods of the orbit; see figure 11(f). Consequently, we stopped the forward Rayleigh number continuation at $Ra = 6407.3$ and do not discuss how PO3 terminates.

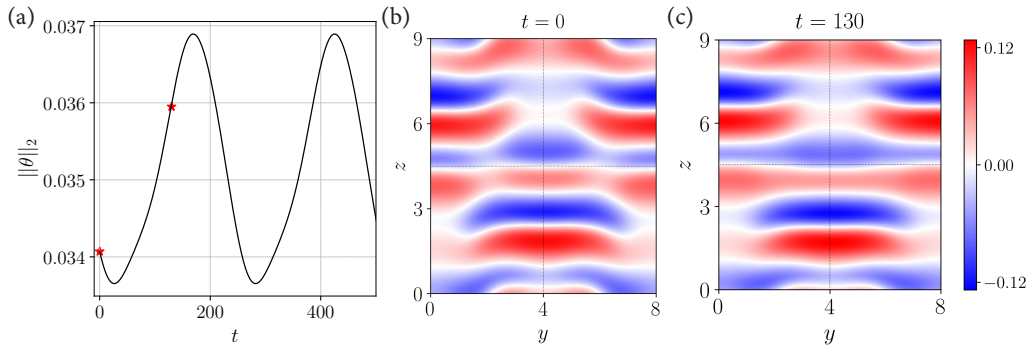


Figure 12: (a) Time series from DNS of PO4 at $Ra = 6300$ ($T = 255.7$). The red stars indicate the moments at which the snapshots (b) and (c) are taken. (b-c) Visualisations of PO4 at $Ra = 6300$, via the temperature field on the y - z plane at $x = 0$.

4.4. Fourth periodic orbit (PO4): Hopf bifurcations

A new periodic orbit PO4 begins and ends on the lower branch of FP6 via two Hopf bifurcations at $Ra = 6257.6$ and $Ra = 6328.8$, respectively. As might be expected and as shown in figure 12, PO4 is an oscillating version of FP6 and preserves its two reflection symmetries $\langle \pi_y, \pi_{xz} \tau(L_y/2, 0) \rangle$. The Hopf bifurcation terminating PO4 occurs very slightly before the saddle-node bifurcation that terminates FP6 at $Ra = 6329$. At $Ra = 6278$, PO4 is destabilized by the occurrence of a secondary Hopf bifurcation. Thus, PO4 is stable for $6257.6 < Ra < 6278$, as shown in figure 4(a) and in the schematic figure 13. Its period increases smoothly and monotonically throughout its range of existence, shown in figure 4(b).

Based on the bifurcation diagram in figure 4(a), the family of branches FP5, FP6, and PO4, are unusual in leaving no trace of their existence beyond the disappearance of FP6 at $Ra = 6329$. Two FP5 branches join and terminate at $Ra = 6317.5$; two FP6 branches, themselves created from FP5, annihilate at $Ra = 6329$; PO4, created from FP6, disappears at $Ra = 6328.8$. When we add to this the disappearances of periodic orbits (PO1 and PO2) via global bifurcations, we see that of the six fixed points and four periodic orbits that arise from the bifurcation of 2D rolls at $Ra = 5707$, only four fixed points and one periodic orbit survive past $Ra = 6329$. Clever & Busse (1995) comments about simplification in another phenomenon (drifting waves) that they observed in vertical convection: “Of course, this is not a physically realistic scenario since there are other bifurcation points on the branch of the steady solutions ... But the return from a complex structure to a more simple one with increasing control parameter is a possibility that cannot be excluded a priori.”

5. Discussion, conclusions and outlook

We have numerically investigated vertical thermal convection in the domain $[L_x, L_y, L_z] = [1, 8, 9]$, the configuration studied by Gao *et al.* (2018), for Rayleigh number up to $Ra \approx 6400$. In this Rayleigh number range, the system exhibits various spatio-temporally organized flow patterns and weak turbulence. Using the computational power of parallelized numerical continuation based on matrix-free Newton methods, we have computed invariant solutions, more specifically fixed points, periodic orbits, and homoclinic and heteroclinic orbits. We have situated all known solutions in the context of a bifurcation diagram.

The bifurcation diagrams shown in figures 2 and 4 are presented in schematic form in figure 13. The schematic diagram contains the names of the states and the bifurcations between

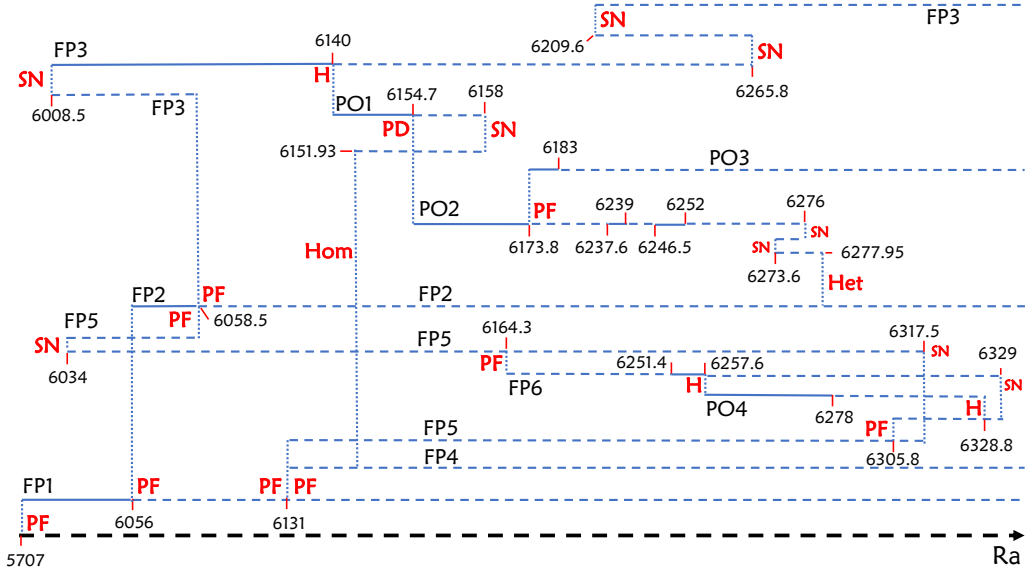


Figure 13: Schematic bifurcation diagram summarizing the origin and stability of all of the fixed points (FPs) and periodic orbits (POs) that we identified in the computational domain $[L_x, L_y, L_z] = [1, 8, 9]$. PF, SN, PD, H, Het and Hom are abbreviations for pitchfork, saddle-node, period-doubling, Hopf, heteroclinic and homoclinic bifurcations. The dotted vertical lines together with the solid red lines and numbers mark the Rayleigh numbers at which bifurcations occur. Solid and dashed horizontal lines signify stable and unstable states respectively.

them, along with their precise thresholds, and emphasizes the complexity of the bifurcation scenario. Compared to the narrow domain $[1, 1, 10]$ presented in [Zheng *et al.* \(2024\)](#), the critical Rayleigh number for the primary instability of four spanwise-independent co-rotating rolls (called FP1 in both papers) in the spanwise-extended domain is only slightly lower. This is due to the slight reduction in the vertical length from $L_z = 10$ to $L_z = 9$ or equivalently from $\lambda = 2.5$ to $\lambda = 2.25$ in the primary roll wavelength. However, secondary and tertiary branches exist at much lower Rayleigh numbers for the $[1, 8, 9]$ domain than for the $[1, 1, 10]$ domain, since the larger domain accommodates a wider variety of spanwise-varying patterns.

We observe complicated bifurcation scenarios involving both spatial and temporal aspects. Spatially, parametric continuation reveals two types of branches. One set of branches consists of states which are aligned with the periodic directions y and z : FP1 (2D rolls), FP2 (diamond rolls), FP5 and the closely related FP6. The other set of branches consists of states which are oriented diagonally: FP3 (thinning rolls) or the similar FP4. We observed two instances of simultaneous bifurcation to branches of states with different symmetries. We were able to explain this otherwise non-generic phenomenon as the breaking of D_4 symmetry of the parent branches FP1 and FP2. (In this highly symmetric geometry, D_4 symmetry is a subgroup of the full symmetry group of FP1 and FP2.) We confirmed this by computing and comparing the eigenvectors responsible for the simultaneous bifurcations.

Temporally, by following certain periodic orbit branches, PO1 and PO2, far from their onset via Hopf and period-doubling bifurcations, we have identified homoclinic and heteroclinic bifurcations that terminate these periodic-orbit branches. The fixed points at which these orbits spend an increasingly long time are aligned with the y, z axes (FP2), or nearly so (FP4), while the excursions are to diagonal states. Thus, these periodic orbits and global bifurcations can also be seen as a manifestation of competition between aligned and diagonal states. Although this is well understood from a mathematical group-theoretic viewpoint, there

should exist some physical or phenomenological interpretation of when and why aligned or diagonal states are favored.

The highest Rayleigh number that we have studied is $Ra = 6407$, 12.3% above the onset of convection (FP1 at $Ra = 5707$). Even in this relatively small range of Ra , we have found a large variety of branches and bifurcation scenarios and there are certainly more to be discovered and analyzed. The increasing number of branches with Rayleigh or Reynolds number is a general feature of the Navier-Stokes and Boussinesq equations. However, branches can also disappear by the same types of local bifurcations that create them, or periodic orbits can be destroyed by global bifurcations. Both of these relatively uncommon scenarios occur in our configuration.

It has been conjectured that trajectories in chaotic and turbulent flows spend a substantial amount of time visiting unstable periodic orbits that are linked via their stable and unstable manifolds (Cvitanović & Eckhardt 1991; Kawahara & Kida 2001). Computing unstable periodic orbits and understanding the bifurcations which produce and link them are thus relevant to better understanding and statistical measures of turbulent flows (Clever & Busse 1995; Chandler & Kerswell 2013; Graham & Floryan 2021).

Acknowledgements. We thank Sajjad Azimi, Florian Reetz and Omid Ashtari for fruitful discussions. We are grateful to Dwight Barkley and to Alastair Rucklidge for their insights on symmetry and to Philippe Beltrame for his suggestions on the robustness of heteroclinic cycles.

Funding. This work was supported by the European Research Council (ERC) under the European Union's Horizon 2020 research and innovation programme (grant no. 865677).

Declaration of interests. The authors report no conflict of interest.

Author ORCID.

Zheng Zheng <https://orcid.org/0000-0002-9833-1347>;

Laurette S. Tuckerman <https://orcid.org/0000-0001-5893-9238>;

Tobias M. Schneider <https://orcid.org/0000-0002-8617-8998>.

REFERENCES

- ABSHAGEN, JAN, LOPEZ, JUAN M, MARQUES, FRANCISCO & PFISTER, GERD 2005 Symmetry breaking via global bifurcations of modulated rotating waves in hydrodynamics. *Phys. Rev. Lett.* **94** (7), 074501.
- BENGANA, YACINE & TUCKERMAN, LAURETTE S. 2019 Spirals and ribbons in counter-rotating Taylor-Couette flow: Frequencies from mean flows and heteroclinic orbits. *Phys. Rev. Fluids* **4**, 044402.
- BERGEON, ALAIN, HENRY, D & KNOBLOCH, E 2001 Three-dimensional Marangoni–Bénard flows in square and nearly square containers. *Physics of Fluids* **13**, 92–98.
- BORDIA, LYES, TUCKERMAN, LAURETTE S, WITKOWSKI, LAURENT MARTIN, NAVARRO, MARÍA CRUZ, BARKLEY, DWIGHT & BESSAIH, RACHID 2010 Influence of counter-rotating von kármán flow on cylindrical rayleigh–bénard convection. *Physical Review E* **81** (3), 036322.
- BOROŃSKA, KATARZYNA & TUCKERMAN, LAURETTE S. 2006 Standing and travelling waves in cylindrical Rayleigh–Bénard convection. *J. Fluid Mech.* **559**, 279–298.
- BUSSE, FH 1978 Non-linear properties of thermal convection. *Reports on Progress in Physics* **41** (12), 1929.
- CHAIT, ARNON & KORPELA, SEPPA A. 1989 The secondary flow and its stability for natural convection in a tall vertical enclosure. *J. Fluid Mech.* **200**, 189–216.
- CHANDLER, GARY J & KERSWELL, RICH R 2013 Invariant recurrent solutions embedded in a turbulent two-dimensional Kolmogorov flow. *J. Fluid Mech.* **722**, 554–595.
- CHOSSAT, PASCAL & IOOSS, GÉRARD 1994 *The Couette-Taylor Problem, Applied Mathematical Sciences*, vol. 102. New York, NY: Springer New York.
- CIMARELLI, ANDREA & ANGELI, DIEGO 2017 Routes to chaos of natural convection flows in vertical channels. *Int. Commun. Heat Mass Transf.* **81**, 201–209.
- CINGI, P, CIMARELLI, A & ANGELI, D 2021 Direct numerical simulation of transition in a differentially heated vertical channel. *International Communications in Heat and Mass Transfer* **126**, 105392.

- CLEVER, R.M. & BUSSE, F.H. 1995 Tertiary and quaternary solutions for convection in a vertical fluid layer heated from the side. *Chaos, Solitons & Fractals* **5**, 1795–1803.
- CVITANOVIĆ, P & ECKHARDT, BRUNO 1991 Periodic orbit expansions for classical smooth flows. *Journal of Physics A: Mathematical and General* **24**, L237–L241.
- DANIELS, KAREN, PLAPP, BRENDAN & BODENSCHATZ, EBERHARD 2000 Pattern Formation in Inclined Layer Convection. *Phys. Rev. Lett.* **84**, 5320–5323.
- DEMAI, Y & IOOSS, G. 1984 Calcul des solutions bifurquées pour le problème de Couette-Taylor avec les 2 cylindres en rotation. *J. Mec. Théor. Appl.* pp. 193–216, special issue.
- GAO, ZHENLAN, PODVIN, BERENGERE, SERGENT, ANNE & XIN, SHIHE 2015 Chaotic dynamics of a convection roll in a highly confined, vertical, differentially heated fluid layer. *Phys. Rev. E* **91**, 1–14.
- GAO, ZHENLAN, PODVIN, BERENGERE, SERGENT, ANNE, XIN, SHIHE & CHERGUI, JALEL 2018 Three-dimensional instabilities of natural convection between two differentially heated vertical plates: Linear and nonlinear complementary approaches. *Phys. Rev. E* **97**, 1–16.
- GAO, ZHENLAN, SERGENT, ANNE, PODVIN, BERENGERE, XIN, SHIHE, LE QUÉRÉ, PATRICK & TUCKERMAN, LAURETTE S. 2013 Transition to chaos of natural convection between two infinite differentially heated vertical plates. *Phys. Rev. E* **88**, 1–18.
- GIBSON, JOHN F, REETZ, FLORIAN, AZIMI, SAJJAD, FERRARO, ALESSIA, KREILOS, TOBIAS, SCHROBSDORFF, HECKE, FARANO, MIRKO, YESIL, AYSE FERHAN, SCHÜTZ, SIMON S, CULPO, MASSIMILIANO & SCHNEIDER, TOBIAS M 2021 Channelflow 2.0. *in preparation* .
- GRAHAM, MICHAEL D. & FLORYAN, DANIEL 2021 Exact Coherent States and the Nonlinear Dynamics of Wall-Bounded Turbulent Flows. *Annu. Rev. Fluid Mech.* **53**, 227–253.
- HALCROW, J., GIBSON, J. F., CVITANOVIĆ, P. & VISWANATH, D. 2009 Heteroclinic connections in plane Couette flow. *J. Fluid Mech.* **621**, 365–376.
- HENRY, DANIEL & BUFFAT, MARC 1998 Two- and three-dimensional numerical simulations of the transition to oscillatory convection in low-Prandtl-number fluids. *J. Fluid Mech.* **374**, 145–171.
- KAWAHARA, GENTA & KIDA, SHIGEO 2001 Periodic motion embedded in plane Couette turbulence: Regeneration cycle and burst. *J. Fluid Mech.* **449**, 291–300.
- KNOBLOCH, E. 1986 Oscillatory convection in binary mixtures. *Phys. Rev. A* **34**, 1538–1549.
- KUZNETSOV, YURI A 2004 *Elements of Applied Bifurcation Theory*, *Applied Mathematical Sciences*, vol. 112. New York, NY: Springer New York.
- MECA, ESTEBAN, MERCADER, ISABEL, BATISTE, ORIOL & RAMÍREZ-PISCINA, LAUREANO 2004 Blue Sky Catastrophe in Double-Diffusive Convection. *Phys. Rev. Lett.* **92**, 259901.
- MILLOUR, E, LABROSSE, G & TRIC, E 2003 Sensitivity of binary liquid thermal convection to confinement. *Physics of Fluids* **15** (10), 2791–2802.
- NAGATA, MASATO & BUSSE, FRIEDRICH H 1983 Three-dimensional tertiary motions in a plane shear layer. *Journal of Fluid Mechanics* **135**, 1–26.
- NORE, C., TUCKERMAN, L. S., DAUBE, O. & XIN, S. 2003 The 1:2 mode interaction in exactly counter-rotating von Kármán swirling flow. *J. Fluid Mech.* **477** (477), 51–88.
- PRAT, JOANA, MERCADER, ISABEL & KNOBLOCH, EDGAR 2002 The 1: 2 mode interaction in rayleigh–bénard convection with and without boussinesq symmetry. *International Journal of Bifurcation and Chaos* **12** (02), 281–308.
- REETZ, FLORIAN 2019 Turbulent patterns in wall-bounded shear flows: invariant solutions and their bifurcations. PhD thesis, Ecole Polytechnique Fédérale de Lausanne.
- REETZ, FLORIAN & SCHNEIDER, TOBIAS M. 2020a Invariant states in inclined layer convection. Part 1. Temporal transitions along dynamical connections between invariant states. *J. Fluid Mech.* **898**, A22.
- REETZ, FLORIAN, SUBRAMANIAN, PRIYA & SCHNEIDER, TOBIAS M. 2020b Invariant states in inclined layer convection. Part 2. Bifurcations and connections between branches of invariant states. *J. Fluid Mech.* **898**, A23.
- SÁNCHEZ, J & NET, M 2010 On the Multiple Shooting Continuation of Periodic Orbits By Newton–Krylov Methods. *Int. Journal of Bifurcation and Chaos* **20**, 43–61.
- SANCHEZ, J., NET, M., GARCIA-ARCHILLA, B. & SIMO, C. 2004 Newton–Krylov continuation of periodic orbits for Navier–Stokes flows. *J. Comput. Phys.* **201**, 13–33.
- SUBRAMANIAN, PRIYA, BRAUSCH, OLIVER, DANIELS, KAREN E., BODENSCHATZ, EBERHARD, SCHNEIDER, TOBIAS M. & PESCH, WERNER 2016 Spatio-temporal patterns in inclined layer convection. *J. Fluid Mech.* **794**, 719–745.
- SWIFT, JAMES WILLIAM 1985 Bifurcation and symmetry in convection. PhD thesis, Univ. Calif. Berkeley.

- TAGG, R., EDWARDS, W. S., SWINNEY, H. L. & MARCUS, P. S. 1989 Nonlinear standing waves in Couette-Taylor flow. *Phys. Rev. A* **39**, 3734.
- TAYLOR, GEOFFREY INGRAM 1923 Stability of a viscous liquid contained between two rotating cylinders. *Phil. Trans. Roy. Soc. London. Series A* **223**, 289–343.
- TUCKERMAN, L S & BARKLEY, D 1988 Global Bifurcations to Traveling Waves in Axisymmetric Convection. *Phys. Rev. Lett.* **61** (4), 408–411.
- VAN VEEN, L, KAWAHARA, G & ATSUSHI, M 2011 On Matrix-Free Computation of 2D Unstable Manifolds. *SIAM Journal on Scientific Computing* **33**, 25–44.
- XIN, SHIHE & LE QUÉRÉ, PATRICK 2002 An extended Chebyshev pseudo-spectral benchmark for the 8: 1 differentially heated cavity. *Int. J. Num. Meth. Fluids* **40**, 981–998.
- ZHENG, ZHENG, TUCKERMAN, LAURETTE S. & SCHNEIDER, TOBIAS M. 2024 Natural convection in a vertical channel. Part 1. Wavenumber interaction and Eckhaus instability in a narrow domain. *submitted to J. Fluid Mech.* .